A strongly coupled oxide-support heterostructure for efficient acidic water oxidation

Hongjun Chen [a], Liming Deng [a], Shuyi Liu [a], Feng Hu *[a], Linlin Li *[a], Jianwei Ren [c] and Shengjie Peng *[a,b]

[a]College of Materials Science and Technology, Nanjing University of Aeronautics and Astronautics, Nanjing 210016, China. E-mail: fenghu@nuaa.edu.cn; lilinlin@nuaa.edu.cn; pengshengjie@nuaa.edu.cn
[b]State Key Laboratory of High Performance Ceramics and Superfine Microstructure, Shanghai 200050, China
[c]Department of Chemical Engineering, University of Pretoria, cnr Lynnwood Road and Roper Street, Hatfield 0028, South Africa. E-mail: jianwei.ren@up.ac.za

Abstract

The synthesized $RuO_2/MnCo_2O_{4.5}$ nano-heterostructure possesses dense interfaces and abundant defect structures, synergistically balancing oxygen evolution reaction (OER) activity and stability. $RuO_2/MnCo_2O_{4.5}$ exhibits a low overpotential of 190 mV at 10 mA cm^{-2}. The proton exchange membrane (PEM) electrolyzer assembled can operate at 200 mA cm^{-2} stably for 50 h.

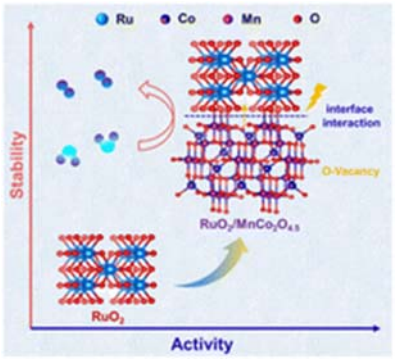

Proton exchange membrane (PEM) electrolyzers have been considered one of the most promising technologies for hydrogen production by water electrolysis because of their characteristics of high efficiency and low energy consumption.[1,2] However, the slow kinetics hinder their large-scale industrial development in water electrolysis.[3–5] Although Ir-based catalysts are always used as the benchmark oxygen evolution reaction (OER) electrocatalysts, Ru-based catalysts are more attractive due to the relatively low-cost and moderate binding ability to oxygen intermediates.[6,7] However, the tendency to be oxidized to Ru^{4+} hinders the large-scale use of Ru-based catalysts.[8] Therefore, developing Ru-based catalysts with both highly catalytic activity and durability to enhance the acid OER kinetics in PEM electrolyzers is the top priority of current research.

Recently, various strategies have been adopted, such as introducing vacancies, doping, and constructing heterogeneous interfaces for RuO_2 modification in PEM water splitting.[9–13] However, balancing the catalytic activity and stability with just a single modulation strategy is difficult. Introducing multiple modulation strategies into the same system is an efficient way to develop efficient Ru-based catalysts.[11] In particular, constructing oxygen vacancies and hetero-interfaces can expose abundant active sites of catalysts and optimize the adsorption strength of critical intermediates, improving the acid OER performance.[11,14] Therefore, it is an effective strategy to introduce interface and defect structures simultaneously.[15] In addition,

adding stable non-precious metals can significantly lower the loading of precious metals and the cost of the catalysts.[16] As a spinel-type transition bimetallic oxide, $MnCo_2O_{4.5}$ is a promising material due to its remarkable electrochemical stability and corrosion resistance in acidic electrolytes.[17] Low conductivity and poor intrinsic activity limit the fast kinetics of $MnCo_2O_{4.5}$.[18] Considering the limitations mentioned above, a feasible and effective strategy is raised that $MnCo_2O_{4.5}$ can be used as a strongly coupled carrier loading RuO_2. The electrons can transfer at the heterogeneous interface between the $MnCo_2O_{4.5}$ and RuO_2 to mitigate excessive oxidation of RuO_2, while introducing oxygen vacancies to enhance electron transport.

Herein, the $RuO_2/MnCo_2O_{4.5}$ heterostructure catalyst is successfully synthesized through hydrothermal and annealing methods. The results of electron paramagnetic resonance (EPR) and X-ray absorption spectroscopy (XAS) confirm that $RuO_2/MnCo_2O_{4.5}$ contains numerous oxygen vacancies and exhibits strong oxide–oxide interface interactions. The nanoparticle structure facilitates the exposure of more active sites, while oxygen vacancies modulate the electron structure, accelerating charge transfer at the interface. The electron supply capacity of the $MnCo_2O_{4.5}$ support can effectively inhibit the excessive oxidation of the Ru site. The presence of heterogeneous interfaces and oxygen vacancies simultaneously enhances the activity and stability of the $RuO_2/MnCo_2O_{4.5}$. The $RuO_2/MnCo_2O_{4.5}$ exhibits an ultralow overpotential of 190 mV to achieve 10 mA cm^{-2} for the OER. The PEM electrolyzer employing $RuO_2/MnCo_2O_{4.5}$ as the anode exhibits a remarkable ability to generate current density of 500 and 1000 mA cm^{-2} at 1.76 and 1.98 V, respectively, and it exhibits excellent durability.

$RuO_2/MnCo_2O_{4.5}$ heterojunction catalyst is successfully synthesized through hydrothermal and calcination annealing (Fig. 1a). X-ray diffraction (XRD) is employed to explore the crystal structure of the catalyst prepared. The diffraction peaks of 31.26°, 36.82°, etc., are from $MnCo_2O_{4.5}$ (JCPDS no. 32-0297). The diffraction angles of 28.02°, 35.06°, and 40.55° correspond to three planes of pure RuO_2 crystals (JCPDS no. 43-1027), respectively, proving the successful synthesis of the $RuO_2/MnCo_2O_{4.5}$ heterojunction catalyst (Fig. 1b). Scanning electron microscopy (SEM) and transmission electron microscopy (TEM) are employed to investigate the morphology and structure of the catalyst. The $MnCo_2O_{4.5}$ precursor adopts a relatively regular cubic shape (Fig. S1, ESI). After the introduction of Ru^{3+}, the previous morphology corrodes and collapses, forming $RuO_2/MnCo_2O_{4.5}$ nanoparticles (Fig. 1c, d and Fig. S2, ESI). Compared to the original cubic structure, the nanoparticles with larger specific surface area can efficiently facilitate exposing abundant active sites. The high-resolution transmission electron microscopy (HRTEM) and the corresponding inverse fast Fourier transform (IFFT) are used further to analyze the interface structure of $RuO_2/MnCo_2O_{4.5}$, revealing that abundant interface structure exists in the catalyst, among which the lattice spacing of 0.254 nm matches well with the (101) plane of RuO_2, while 0.285 nm corresponds to the (220) plane of $MnCo_2O_{4.5}$ (Fig. 1e and f). Electron interaction at the heterojunction interface can efficiently promote the adsorption/desorption of the reaction intermediates. The overlap of lattice fringes of $MnCo_2O_{4.5}$ and RuO_2 demonstrates the atom coupling, which can enhance interaction at the interface and improve the conductivity.[19,20] Additionally, elemental mapping of $RuO_2/MnCo_2O_{4.5}$ reveals that the elements of Co, Mn, O, and Ru are uniformly distributed in the catalyst (Fig. 1g). The above analyses have verified the successful formation of the $RuO_2/MnCo_2O_{4.5}$ heterojunction catalyst.

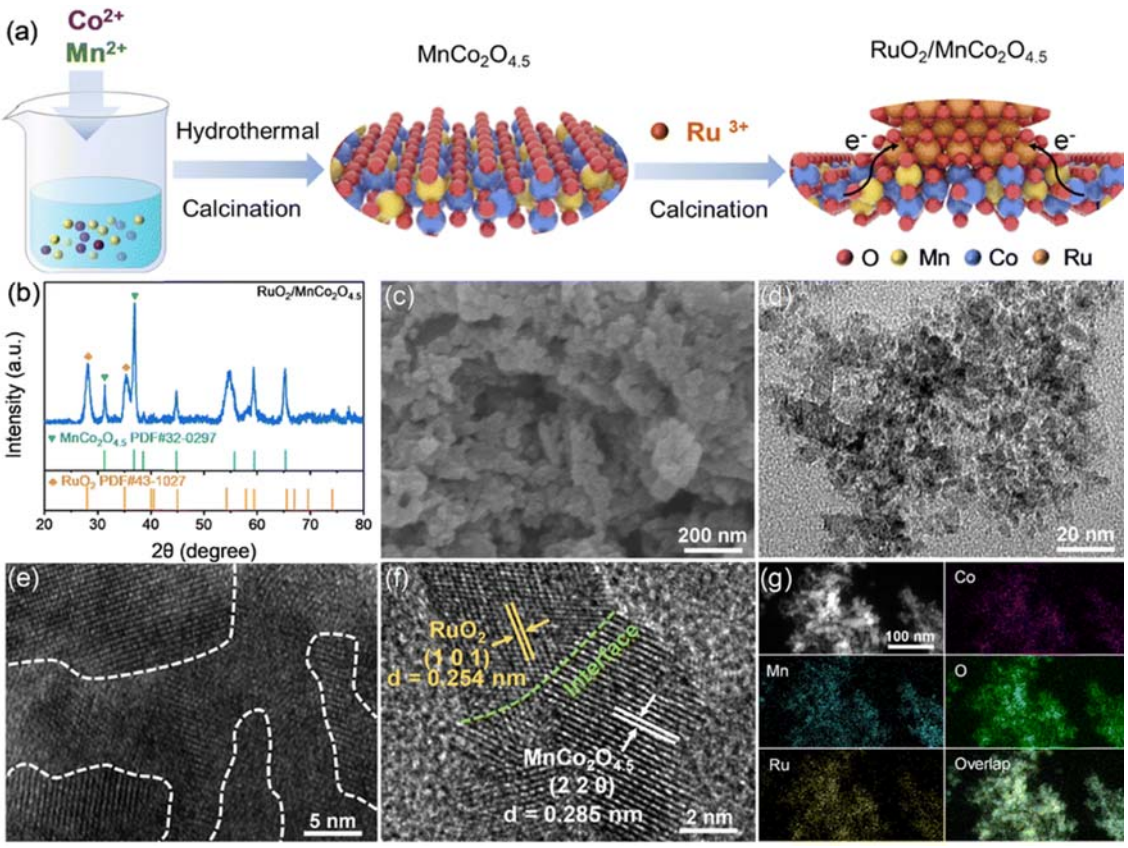

Fig. 1 (a) Schematic illustration of the synthesis of $RuO_2/MnCo_2O_{4.5}$. (b) XRD pattern, (c) SEM image, (d) and (e) TEM images, and (f) HRTEM image of $RuO_2/MnCo_2O_{4.5}$. (g) EDS elemental mapping of Co, Mn, Ru, and O in $RuO_2/MnCo_2O_{4.5}$.

The coupling effect between RuO_2 and $MnCo_2O_{4.5}$ is investigated by X-ray photoelectron spectroscopy (XPS) measurement. The XPS spectra demonstrate the successful synthesis of $RuO_2/MnCo_2O_{4.5}$ (Fig. S3, ESI). As shown in Fig. 2a and b, compared with $MnCo_2O_{4.5}$, the Co 2p binding energy in $RuO_2/MnCo_2O_{4.5}$ positively shifts by 0.2 eV, while the Mn 2p peaks negatively shift by 0.2 eV, revealing electron transfer at the interface between the RuO_2 and $MnCo_2O_{4.5}$ or inside the $MnCo_2O_{4.5}$. Additionally, the Ru 3p peak in $RuO_2/MnCo_2O_{4.5}$ positively shifts by 0.5 eV compared to commercial RuO_2 (Fig. 2c). Some electrons are transferred from Co/Ru atoms to Mn, causing the electron density around Mn to increase.[21,22] The above XPS data demonstrate that there is a strong electronic coupling interaction between RuO_2 and $MnCo_2O_{4.5}$, which can inhibit the oxidation and dissolution of Ru sites, improving the durability.[23] The $RuO_2/MnCo_2O_{4.5}$ shows symmetric peaks on both sides of the g-factor of 2.003, and exhibits a strong EPR signal, suggesting that abundant oxygen vacancies exist (Fig. S4, ESI).[24] The O 1s XPS spectra can be assigned to absorbed oxygen and lattice oxygen, which are located at 531.97 and 529.23 eV, respectively (Fig. S5, ESI). After the composition of the $RuO_2/MnCo_2O_{4.5}$, it can be observed that the intensity of adsorption oxygen closely related to surface oxygen vacancies increases, which is consistent with the results of EPR.

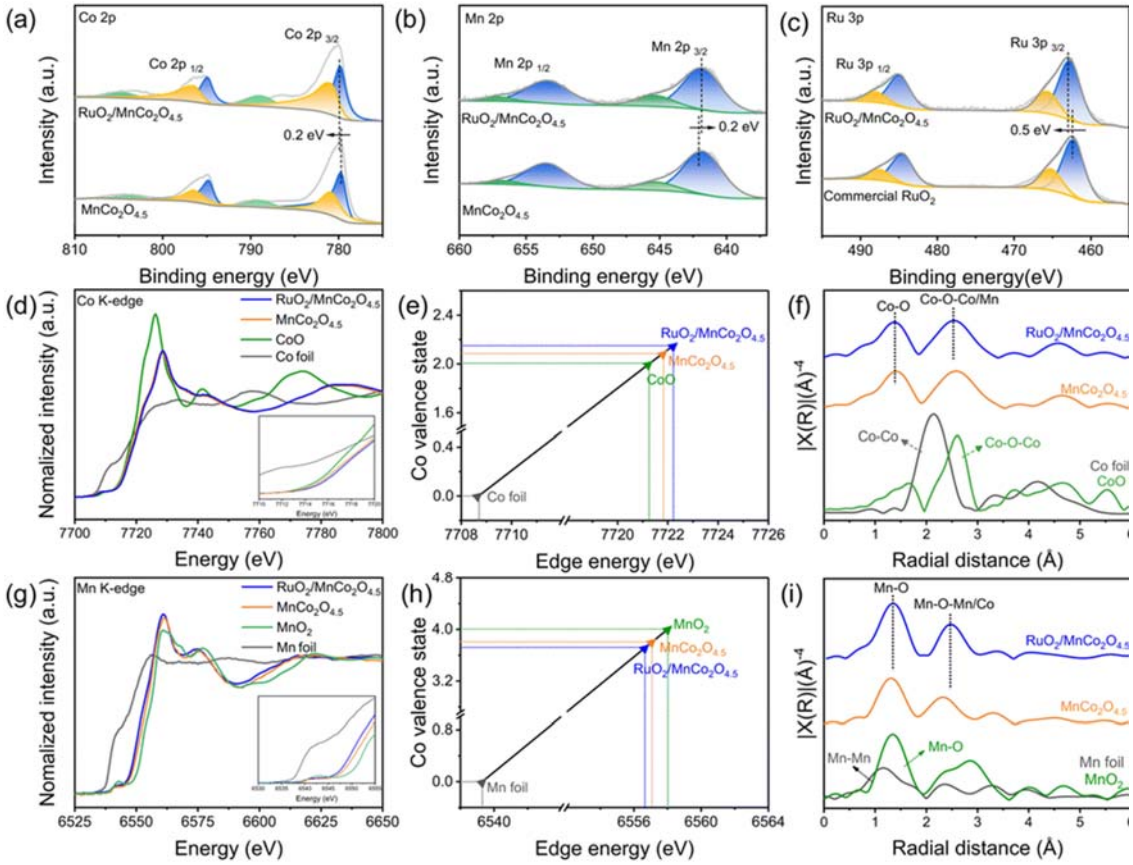

Fig. 2 (a) Co 2p XPS spectra, and (b) Mn 2p XPS spectra of $MnCo_2O_{4.5}$ and $RuO_2/MnCo_2O_{4.5}$. (c) Ru 3p XPS spectra of commercial RuO_2 and $RuO_2/MnCo_2O_{4.5}$. (d) The normalized XANES spectra, (e) relation between the Co K-edge absorption energy (E_0) and valence state, (f) FT-EXAFS spectrum at the Co-edge for Co foil, CoO, $MnCo_2O_{4.5}$ and $RuO_2/MnCo_2O_{4.5}$. (g) The normalized XANES spectra, (h) relation between the Co K-edge absorption energy (E_0) and valence state, and (i) FT-EXAFS spectrum at the Mn-edge for Mn foil, MnO_2, $MnCo_2O_{4.5}$ and $RuO_2/MnCo_2O_{4.5}$.

XAS is employed to investigate the alterations in the electronic structure and coordination environment of Co and Mn sites in $RuO_2/MnCo_2O_{4.5}$. Significantly, the Co K-edge position of the $RuO_2/MnCo_2O_{4.5}$ heterojunction catalyst shifts to higher energy compared to CoO, and the pre-edge intensity is slightly higher than that of $MnCo_2O_{4.5}$, which corresponds with the XPS results (Fig. 2d).[25] Upon the formation of the $RuO_2/MnCo_2O_{4.5}$ heterojunction catalyst, the electron density around the Co sites decreases, which indicates strong coupling between the RuO_2 and $MnCo_2O_{4.5}$. The oxidation state of Co in the $RuO_2/MnCo_2O_{4.5}$ (2.15) is higher than that in CoO and $MnCo_2O_{4.5}$ (2.09) (Fig. 2e and Fig. S6, S7, ESI). The Co K-edge extended X-ray absorption fine structure (EXAFS) oscillations in R-space and wavelet transform (WT) reveal two prominent coordination peaks at 1.39 and 2.52 Å in $RuO_2/MnCo_2O_{4.5}$, which corresponds with Co–O and Co–O–Co/Mn bonds, respectively (Fig. 2f and Fig. S8, ESI). In Mn K-edge XANES spectra, the near-edge absorption energy of Mn in $RuO_2/MnCo_2O_{4.5}$ is lower than that in $MnCo_2O_{4.5}$, indicating a decrease in the oxidation state of Mn after forming the composition (Fig. 2g, h and Fig. S9 and S10, ESI). The Mn K-edge extended X-ray absorption fine structure (EXAFS) spectra exhibit peaks at 1.34 and 2.46 Å, corresponding to Mn–O and Mn–Mn/Co bonds, respectively (Fig. 2i). This phenomenon indicates that the environment around the Mn sites has been changed, which is possibly caused by oxygen

vacancies.[26] All these findings are further demonstrated by the wavelet transform spectrum (Fig. S11, ESI).

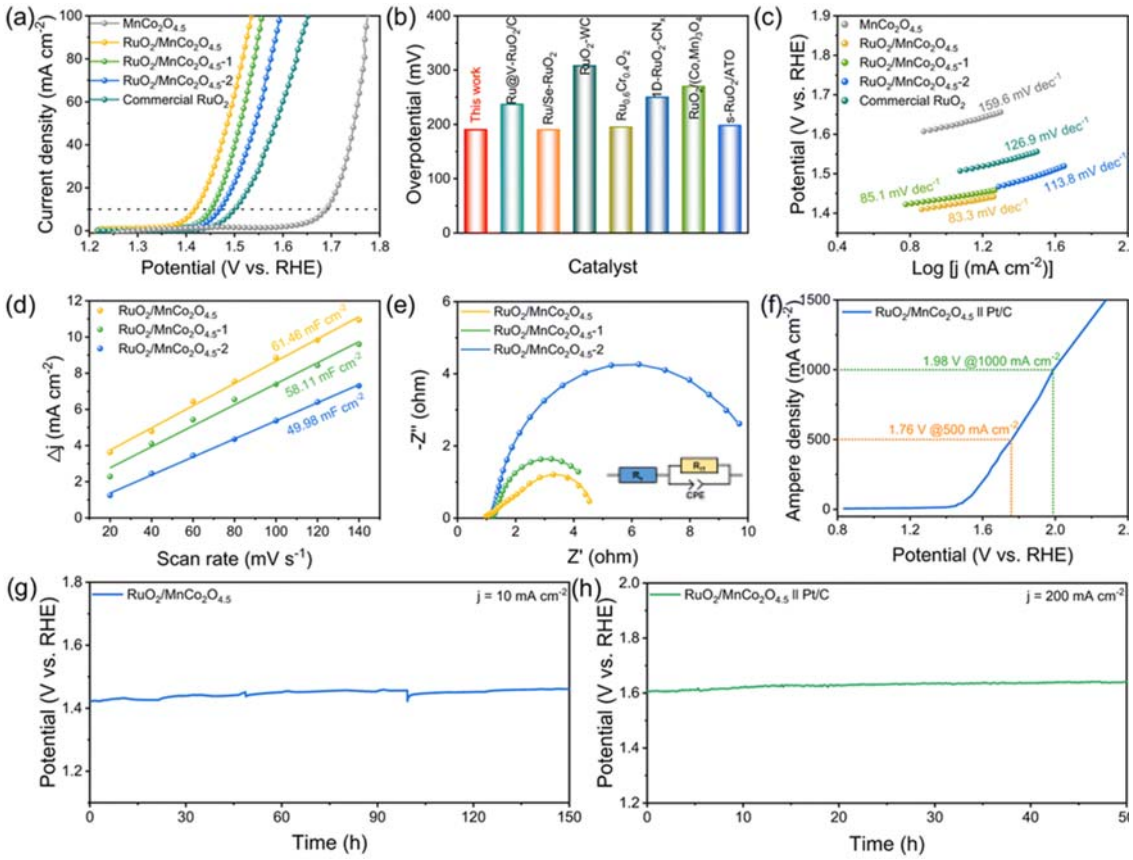

Fig. 3 (a) LSV curves. (b) Comparison of the overpotentials of $RuO_2/MnCo_2O_{4.5}$ and other reported catalysts in 0.5 M H_2SO_4. (c) Tafel plots. (d) C_{dl} values. (e) Nyquist plots and equivalent circuit. (f) Overall water splitting performance of $RuO_2/MnCo_2O_{4.5}$‖Pt/C. (g) Long-term chronopotentiometry curve of $RuO_2/MnCo_2O_{4.5}$ at 10 mA cm^{-2}. (h) Chronopotentiometry curve for the PEM electrolyzer cell of $RuO_2/MnCo_2O_{4.5}$‖Pt/C.

The OER performance of $RuO_2/MnCo_2O_{4.5}$ is assessed by a typical standard three-electrode device in 0.5 M H_2SO_4. After coupling the $MnCo_2O_{4.5}$ with different RuO_2 content, the catalysts prepared exhibit excellent acidic OER activity (Fig. 3a). The $RuO_2/MnCo_2O_{4.5}$ provides a small η_{10} of 190 mV, much better than that of $RuO_2/MnCo_2O_{4.5}$-1 (220 mV), $RuO_2/MnCo_2O_{4.5}$-2 (240 mV), RuO_2 (270 mV), and $MnCo_2O_{4.5}$ (458 mV). The $RuO_2/MnCo_2O_{4.5}$ is superior to most acidic OER RuO_2-based catalysts reported (Fig. 3b and Table S1, ESI). The mass activity for $RuO_2/MnCo_2O_{4.5}$ is 636.2 and 1515.7 A g^{-1} at overpotentials of 270 and 347 mV, respectively, which is superior to most acidic OER RuO_2-based catalysts (Fig. S12 and Table S2, ESI). To deeply analyze the reaction kinetics of the OER process, the Tafel slope is examined within the linear region. As shown in Fig. 3c, the Tafel slope value of $RuO_2/MnCo_2O_{4.5}$ is determined only to be 83.3 mV dec^{-1}, suggesting that the heterojunction interface and oxygen vacancies accelerate the reaction kinetics.[27] Cyclic voltammetry is utilized to calculate the double-layer capacitance (C_{dl}) to reveal the electrochemical activity in OER processes (Fig. S13, ESI). The results indicate that $RuO_2/MnCo_2O_{4.5}$ exhibits the largest C_{dl} (61.46 mF cm^{-2}) (Fig. 3d). The OER polarization curves normalized by the ECSA show that the intrinsic activity of $RuO_2/MnCo_2O_{4.5}$ is the best

(Fig. S14, ESI). The Nyquist plots demonstrate that $RuO_2/MnCo_2O_{4.5}$ exhibits the lowest charge transfer resistance of 0.91, indicating that charge transfer at the interface between the catalyst and electrolyte is improved (Fig. 3e).[28] Furthermore, durability is another important factor in assessing the electrochemical performance. $RuO_2/MnCo_2O_{4.5}$ exhibits only a slight voltage loss after 150 h at 10 mA cm^{-2} in 0.5 M H_2SO_4, while commercial RuO_2 lost all OER activity rapidly within 5 h (Fig. 3g and Fig. S15, ESI). The SEM and XRD tests show that the $RuO_2/MnCo_2O_{4.5}$ after the continuous operation well retains the nanoparticle structure and original phase (Fig. S16, ESI).

To explore the practical application of $RuO_2/MnCo_2O_{4.5}$ in water electrolysis, we assembled a PEM electrolyzer under industrial conditions (Fig. S17, ESI).[29] Notably, the PEM electrolyzer assembled by using $RuO_2/MnCo_2O_{4.5}$ and Pt/C as the anode and cathode, respectively, required only 1.76 and 1.98 V to deliver 500 and 1000 mA cm^{-2} in the acidic electrolyte, respectively (Fig. 3f). Moreover, the electrolyzer can operate continuously for 50 h at 200 mA cm^{-2} without significant degradation (Fig. 3h). The $RuO_2/MnCo_2O_{4.5}$ exhibits remarkable performance in PEM water electrolysis, comparable to several recent catalysts reported (Table S3, ESI). All the results confirm the high efficiency of $RuO_2/MnCo_2O_{4.5}$ for PEM electrolysis.

Standard cyclic voltammetry (CV) scans are conducted on the catalysts to explore the formation and characteristics of the active sites during the acidic OER. Compared to the reversible hydrogen electrode (RHE), the CV of commercial RuO_2 exhibits two pairs of redox peaks corresponding to the surface redox transitions of Ru^{3+}/Ru^{4+} (0.64 V) and Ru^{4+}/Ru^{5+} (1.24 V), respectively (Fig. 4a).[1,30] In contrast, with a rapid increase of redox current, the $RuO_2/MnCo_2O_{4.5}$ exhibits a weaker redox peak at 1.24 V, implying that the excessive oxidation of Ru sites is effectively suppressed. In situ EIS tests are conducted at diverse voltage conditions to investigate the kinetics of the OER process further.[30] The phase angle of commercial RuO_2 at high frequency is comparable to that of $RuO_2/MnCo_2O_{4.5}$, indicating a similar electron conduction ability in the inner layers (Fig. 4b and c). Inversely, in the low-frequency region, the smaller phase angle of $RuO_2/MnCo_2O_{4.5}$ illustrates a faster charge transfer rate occurring at the electrolyte-catalyst interface (Fig. S18, ESI). Overall, the $RuO_2/MnCo_2O_{4.5}$ is more sensitive to the potential response, indicating faster adsorption kinetics during the acidic OER. Furthermore, XPS is conducted on the $RuO_2/MnCo_2O_{4.5}$ after operation. The Co 2p and Mn 2p significantly shift towards positive binding energy, while Ru 3p exhibits only a 0.5 eV positive shift (Fig. 4d, e and Fig. S19, ESI). The electron transfer from Co and Mn sites to Ru effectively prevents the formation of high-valent Ru (Fig. S20, ESI). Moreover, $RuO_2/MnCo_2O_{4.5}$ demonstrates pH-independent OER kinetics, with the current densities remaining nearly constant across different pH values, exhibiting a potential adsorbate evolution mechanism (AEM) (Fig. S21, ESI). In situ Raman spectroscopy measurements are conducted to probe the dynamic surface structure evolution of the catalyst during the OER (Fig. 4f). The vibrational peaks for Ru–O and Co–O bands appear at 500–700 cm^{-1} throughout the potential window. As the voltage increases, no shift appears in the Ru–O and Co–O bands, indicating stable bonding under high-voltage conditions. The high-valence Ru gradually forms, and a *OOH intermediate participates in the reaction, which aligns with the AEM mechanism, avoiding the involvement of lattice oxygen and improving the stability.[31]

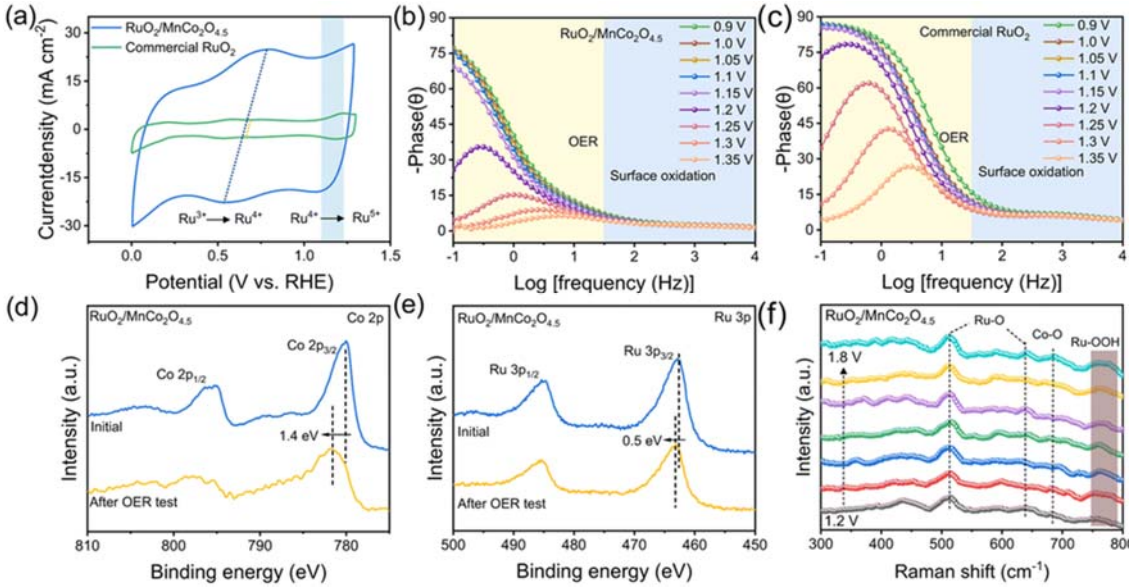

Fig. 4 (a) Typical CV curves, (b) and (c) Bode phase plots of $RuO_2/MnCo_2O_{4.5}$ and commercial RuO_2. (d) Co 2p, and (e) Ru 3p XPS spectra of $RuO_2/MnCo_2O_{4.5}$ before and after the OER test. (f) In situ electrochemical Raman spectra recorded on $RuO_2/MnCo_2O_{4.5}$ in H_2SO_4.

In summary, we successfully synthesized a $RuO_2/MnCo_2O_{4.5}$ heterojunction catalyst with rich oxygen vacancies. The $RuO_2/MnCo_2O_{4.5}$ possesses large specific surface area, which is beneficial for exposing more active sites. Importantly, the introduction of oxygen vacancies exposes more active sites, improving the intrinsic activity of the catalyst. Meanwhile, the $MnCo_2O_{4.5}$ support can supply extra electrons to RuO_2 through the interface during the OER, protecting the Ru sites from excessive oxidation. The $RuO_2/MnCo_2O_{4.5}$ displays remarkable OER performance with an overpotential of 190 mV at 10 mA cm^{-2} and exhibits almost no degradation even after 150 h of continuous operation. In addition, the PEM assembled using $RuO_2/MnCo_2O_{4.5}$ as the anode operates stably for 50 h at 200 mA cm^{-2}. This study lays a foundation for the preparation of efficient electrocatalysts in acidic water electrolysis.

This work was supported by the National Natural Science Foundation of China (22075141 and 52371226), the Open Foundation of Shanghai Jiao Tong University Shaoxing Research Institute of Renewable Energy and Molecular Engineering (Grant No. JDSX2023019), the Opening Project of State Key Laboratory of High Performance Ceramics and Superfine Microstructure (SKL202208SIC), Postgraduate Research & Practice Innovation Program of NUAA (xcxjh20230603), and the Natural Science Foundation of Jiangsu Province (BK20210311).

Data availability

The data supporting this article have been included as a part of the ESI.

Conflicts of interest

There are no conflicts to declare.

Notes and references

1. L. Deng, S.-F. Hung, Z.-Y. Lin, Y. Zhang, C. Zhang, Y. Hao, S. Liu, C.-H. Kuo, H.-Y. Chen, J. Peng, J. Wang and S. Peng, Adv. Mater., 2023, 35, 2305939.
2. S. Shen, Z. Wang, Z. Lin, K. Song, Q. Zhang, F. Meng, L. Gu and W. Zhong, Adv. Mater., 2022, 34, e2110631.
3. H. Wu, Q. Lu, Y. Li, M. Zhao, J. Wang, Y. Li, J. Zhang, X. Zheng, X. Han, N. Zhao, J. Li, Y. Liu, Y. Deng and W. Hu, J. Am. Chem. Soc., 2023, 145, 1924.
4. S. Hao, H. Sheng, M. Liu, J. Huang, G. Zheng, F. Zhang, X. Liu, Z. Su, J. Hu, Y. Qian, L. Zhou, Y. He, B. Song, L. Lei, X. Zhang and S. Jin, Nat. Nanotechnol., 2021, 16, 1371–1377.
5. C. Fan, X. Wu, M. Li, X. Wang, Y. Zhu, G. Fu, T. Ma and Y. Tang, Chem. Eng. J., 2022, 431, 133829.
6. Z. Wang, B. Xiao, Z. Lin, Y. Xu, Y. Lin, F. Meng, Q. Zhang, L. Gu, B. Fang, S. Guo and W. Zhong, Angew. Chem., Int. Ed., 2021, 60, 23388.
7. W. Wang, Z. Wang, Y. Hu, Y. Liu and S. Chen, eScience, 2022, 2, 438.
8. K. Du, L. Zhang, J. Shan, J. Guo, J. Mao, C.-C. Yang, C.-H. Wang, Z. Hu and T. Ling, Nat. Commun., 2022, 13, 5448.
9. S. C. Sun, H. Jiang, Z. Y. Chen, Q. Chen, M. Y. Ma, L. Zhen, B. Song and C. Y. Xu, Angew. Chem., Int. Ed., 2022, 61, e202202519.
10. G. Zhao, K. Rui, S. X. Dou and W. Sun, Adv. Funct. Mater., 2018, 28, 1803291.
11. H. Liu, J. Miao, Y. Wang, S. Chen, Y. Tang and D. Zhu, Chem. Commun., 2024, 60, 4443–4446.
12. X. Xu, Y. Zhong, M. Wajrak, T. Bhatelia, S. P. Jiang and Z. Shao, InfoMat, 2024, 6, e12608.
13. J. Huang, H. Sheng, R. D. Ross, J. Han, X. Wang, B. Song and S. Jin, Nat. Commun., 2021, 12, 3036.
14. X. Cui, P. Ren, C. Ma, J. Zhao, R. Chen, S. Chen, N. P. Rajan, H. Li, L. Yu, Z. Tian and D. Deng, Adv. Mater., 2020, 32, 1908126.
15. J. Sun, H. Xue, Y. Zhang, X.-L. Zhang, N. Guo, T. Song, H. Dong, Y. Kong, J. Zhang and Q. Wang, Nano Lett., 2022, 22, 3503.
16. S. Wang, X. Ning, Y. Cao, R. Chen, Z. Lu, J. Hu, J. Xie and A. Hao, Inorg. Chem., 2023, 62, 6428–6438.
17. B. Wang, S. Wang, Y. Tang, C.-W. Tsang, J. Dai, M. K. H. Leung and X.-Y. Lu, Appl. Energy, 2019, 252, 113452.
18. J. Li, N. Zhou, H. Wang, H. Li, Z. Xie, H. Chu, Y. Tang, L. Sun and Z. Peng, J. Electrochem. Soc., 2015, 162, A2302–A2307.
19. Y. Gao, D. Zheng, Q. Li, W. Xiao, T. Ma, Y. Fu, Z. Wu and L. Wang, Adv. Funct. Mater., 2022, 32, 2203206.
20. N. Yao, Z. Fan, Z. Xia, F. Wu, P. Zhao, G. Cheng and W. Luo, J. Mater. Chem. A, 2021, 9, 18208–18212.
21. C. Zheng, B. Huang, X. Liu, H. Wang and L. Guan, Inorg. Chem. Front., 2024, 11, 1912–1922.
22. Z. Wang, Z. Lin, J. Deng, S. Shen, F. Meng, J. Zhang, Q. Zhang, W. Zhong and L. Gu, Adv. Energy Mater., 2020, 11, 2003023.
23. R. Ge, L. Li, J. Su, Y. Lin, Z. Tian and L. Chen, Adv. Energy Mater., 2019, 9, 1901313.
24. G. Zhao, Z. Luo, B. Zhang, Y. Chen, X. Cui, J. Chen, Y. Liu, M. Gao, H. Pan and W. Sun, Nano Res., 2023, 16, 4767–4774.
25. L. Li, G. Zhang, J. Xu, H. He, B. Wang, Z. Yang and S. Yang, Adv. Funct. Mater., 2023, 33, 2213304.

26. L. Zhang, H. Jang, H. Liu, M. G. Kim, D. Yang, S. Liu, X. Liu and J. Cho, Angew. Chem., Int. Ed., 2021, 60, 18821–18829.
27. H. Jin, S. Choi, G. J. Bang, T. Kwon, H. S. Kim, S. J. Lee, Y. Hong, D. W. Lee, H. S. Park, H. Baik, Y. Jung, S. J. Yoo and K. Lee, Energy Environ. Sci., 2022, 15, 1119–1130.
28. S. Hao, M. Liu, J. Pan, X. Liu, X. Tan, N. Xu, Y. He, L. Lei and X. Zhang, Nat. Commun., 2020, 11, 5368.
29. X. Xu, H. Sun, S. P. Jiang and Z. Shao, SusMat, 2021, 1, 460–481.5.
30. L. Deng, S. Liu, D. Liu, Y. M. Chang, L. Li, C. Li, Y. Sun, F. Hu, H. Y. Chen, H. Pan and S. Peng, Small, 2023, 19, e2302238.
31. X. Wang, X. Wan, X. Qin, C. Chen, X. Qian, Y. Guo, Q. Xu, W. Cai, H. Yang and K. Jiang, ACS Catal., 2022, 12, 9437–9445.